Delft University of Technology

Exploring the impact of different inflow conditions on wind turbine wakes using Large-Eddy Simulations

Parinam, Anand; Benard, Pierre; Von Terzi, Dominic; Viré, Axelle

Important note
To cite this publication, please use the final published version (if applicable).
Please check the document version above.

PAPER • OPEN ACCESS

Exploring the impact of different inflow conditions on wind turbine wakes using Large-Eddy Simulations

To cite this article: Anand Parinam *et al* 2024 *J. Phys.: Conf. Ser.* **2767** 092098

View the article online for updates and enhancements.

Exploring the impact of different inflow conditions on wind turbine wakes using Large-Eddy Simulations

Anand Parinam[1,2], Pierre Benard[2], Dominic von Terzi[1] and Axelle Viré[1]

[1] Faculty of Aerospace Engineering, Delft University of Technology, The Netherlands
[2] CORIA, CNRS UMR6614, Normandie Université, INSA and University of Rouen, 76801 Saint-Etienne-du-Rouvray, France.

E-mail: `A.parinam@tudelft.nl`

Abstract.
The ever-growing demand for renewable energy, driven by cost-effectiveness and minimal ecological impacts, has resulted in the deployment of larger wind turbines with rotor diameters surpassing 200 m. This underscores the importance of a thorough understanding of flow dynamics to optimize operational efficiency in diverse atmospheric inflow scenarios. Understanding the intricate impact of atmospheric conditions, including wind shear and turbulence, on wind turbine wakes is crucial for optimizing wind farm layouts and performance, influencing wake evolution, turbine loads, and power output. This research focuses on bridging the gap between idealized inflow scenarios and real-world atmospheric inflow conditions by systematically integrating linear shear, turbulence and the logarithmic wind shear profile into the uniform inflow conditions and analyzing the wake behind the IEA-15 MW wind turbine. To specifically examine inflow effects, a constant hub height wind speed was maintained through a velocity controller. The study focuses on analyzing the wake's flow field and providing insights into its recovery process. It was found that turbulence plays a critical role in a faster wake recovery as well as increasing the power production of the turbine for sheared inflows and the wind speed selected.

1. Introduction

The increasing demand for energy and the decreasing costs of renewable electricity sources, particularly wind and solar energy, have led to a significant expansion in their deployment. This growth has prompted the development of larger and higher-rated wind turbines, with rotor diameters exceeding 200 m. The performance of these large turbines exhibits significant variation throughout the diurnal cycle due to diverse atmospheric conditions [1, 2, 3]. Consequently, a comprehensive understanding of the flow fields around wind turbines under various atmospheric conditions is essential for accurately predicting performance and efficiently operating wind farms and turbines [4].

Atmospheric flows contain a large number of temporal and spatial structures, whose variations impact wind turbine wakes in the velocity-deficit region downstream of the turbine due to blade rotation [5]. Understanding atmospheric conditions and the impact on turbine wakes is crucial for optimizing wind farm layouts [6]. In stable atmospheric conditions characterized by high shear and low turbulence, turbine wakes persist over longer distances compared to the often-studied neutral conditions, resulting in a more pronounced impact on downstream

waked turbines [7]. The presence of high wind shear has a twofold impact on wake evolution and turbine performance, affecting wake size, shape, and recovery, and impacting loads and power output [8]. Hodgkin et al. [9] demonstrated that shear significantly impacts the evolution of tip vortices and, consequently, the shape of the wake. Furthermore, wind shear and turbulence can lead to the formation of highly complex wake structures downstream of the turbine rotor, characterized by significant asymmetries, streamwise vorticity generation, non-periodicity, and non-uniformity [10]. The examination of wind turbine responses to the wind shear and turbulence in the atmospheric boundary layer (ABL) has been explored to a certain degree [3, 11, 12, 13]. The impact of wind shear and turbulence on power generation has been investigated by highlighting the differences in turbine performance [14, 15]. Additionally, the turbulence structure and intensity distribution in the wake have been shown to affect the fatigue loading of downwind turbines [16]. The interaction of turbine rotors with this complex wake flow field in wind farms may lead to significant power losses due to wake effects [17].

This research is an extension of Parinam et al. [8] which investigated the influence of wind shear on wind turbine wakes under simplified idealized inflow conditions. In this study, additional physical elements are systematically integrated, such as turbulence and the log-law shear profile, into these simplistic conditions to bridge the gap between idealized inflow scenarios and real-world atmospheric inflow conditions. Incorporating each element within the inflow conditions in a high-fidelity Large-Eddy Simulation (LES) approach aims to facilitate the identification of their respective impacts on the characteristics of wakes, such as wake recovery, as well as on turbine performances. This paper addresses the significance of the presence of turbulence and the impact of idealizing conditions, aiming to answer the question of their importance in wind turbine wake studies.

The paper is organized as follows. Section 2 reviews the methodology, encompassing the governing equations and implementation of turbine simulations for both precursor and turbine simulations. Concise results for the analyzed test cases are presented in Section 3. Lastly, Section 4 summarizes the main findings and serves as the conclusion of the paper.

2. Methodology

2.1. Governing equations

LES analysis of the flow around a single three-bladed turbine is conducted using YALES2, a massively parallelized CFD platform [18]. YALES2 solves the three-dimensional incompressible filtered Navier-Stokes equations, employing 4th-order time and space integration schemes. The governing equations are given by:

$$\frac{\partial \widetilde{u}_j}{\partial x_j} = 0 \tag{1}$$

$$\frac{\partial \widetilde{u}_i}{\partial t} + \frac{\partial}{\partial x_j}(\widetilde{u}_i \widetilde{u}_j) = -\frac{1}{\rho}\frac{\partial \widetilde{p}}{\partial x_i} + \frac{\partial \widetilde{\tau}_{ji}}{\partial x_j} - \frac{\partial}{\partial x_j}(2\rho \nu_{sgs} \widetilde{S^*_{ij}}) + F_p \tag{2}$$

where $\widetilde{u}_i$ is the filtered velocity field, $\widetilde{p}$ the filtered pressure field, ν_{sgs} is the sub-grid scale kinematic viscosity and $\widetilde{S^*_{ij}}$ is the strain rate tensor. In this work, ν_{sgs} is modeled according to the Smagorinsky model [19] with Smagorinsky coefficient $C_s = 0.16$. The body force F_p in Eq. (2) represents the effect of the wind turbine on the flow. This term is modeled by using the Actuator Line Method (ALM) in the framework developed by Shen & Sorensen [20].

2.2. Turbine Simulations

The turbine simulations are performed using the IEA 15MW reference wind turbine [21]. Here, x denotes the streamwise flow direction, y is the spanwise and z is the vertical direction. The rotor diameter is $D = 240$ meters. The turbine rotor is placed at $3D$ downstream of the inlet and mid-span ($5D$) of the computational domain with size 18D × 10D × 6D. An unstructured mesh

Cases	Inflow condition	Characteristics
1	No Shear	Laminar inflow velocity $8m/s$
2	Uniform Linear Shear	Wind Shear Coefficient $\alpha = 0.2$
3	Turbulent Linear Shear	Case 2 + Turbulence (from Case 4)
4	Turbulent Log-Law	Logarithmic wind profile with $Z_0 = 0.02$ and hub-height velocity $= 8m/s$

Table 1: Description of inflow conditions employed in this research.

with refinement near the turbine wake is used where the cell size is $D/\Delta x = 120$, accounting for around 630 million tetrahedra. The length of the refinement zone is 12D. The rotor blades are discretized in the spanwise direction into 64 points and the smearing factor is defined as $\epsilon/\Delta x = 2$. The simulation is advanced for a standard 10-minute interval [22] for stabilization of transients and subsequently, 10 min interval to compute the statistical quantities in the wake of the turbine with a time step of 0.04 s. Additionally, the presence of the nacelle is excluded based on the insights from a study on its limited effect on the near and far-wake [8].

In this work, four cases are studied with the wind turbine being exposed to different inflow conditions, as summarized in Table 1 and detailed below.

Case 1

The wind turbine is subjected to a uniform inflow with a velocity of $8m/s$. The inflow does not have any shear nor turbulence. Slip walls are used for the y- and z-directions, whereas inflow-outflow boundary conditions are prescribed in the x-direction. The turbine is positioned with its hub at $3D$ along the height z.

Case 2

A linear shear profile replaces the uniform inflow of Case 1 and ensures a hub-height velocity of $8m/s$ (i.e. u_{ref} is $8m/s$ at a height of $150m$). The simplified shear conditions are imposed via a uniform vertical velocity gradient at the inlet. This linear vertical velocity profile is presented in Eq. (3), whose slope is obtained using the well-known power law [23] for a wind shear coefficient of 0.2.

$$u(z) = u_{ref} * (1 + \alpha \frac{z}{h_{ref}}) \tag{3}$$

Case 3

Turbulent fluctuations are added to the linear shear of Case 2 along with the same boundary conditions. The turbulent fluctuations are generated by adapting the precursor simulation to the linear shear profile as explained below. The precursor simulation generates a turbulent logarithmic profile in YALES2 using Eq. 4. The implementation of inflow turbulence for the scenario of linear shear with turbulence is illustrated in Figure 1. The turbulent z-planes obtained from the logarithmic precursor database for each height are utilized to calculate the average logarithmic velocity profile along the z-axis. Subsequently, this average profile is subtracted from the database to derive a turbulent box consisting of x-planes with turbulent fluctuations. Additionally, a linear shear profile with a wind shear coefficient (WSC) of 0.2 is incorporated into the remaining box of fluctuations.
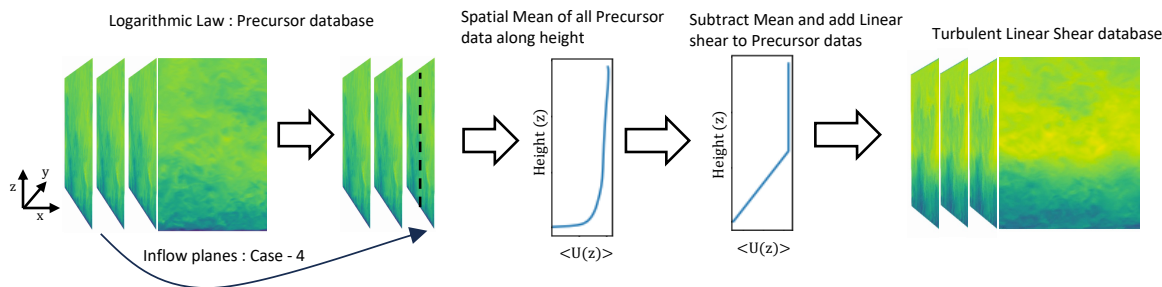
Figure 1: Schematic of implementation of inflow turbulence generation for Case 3.

$$u(z) = \frac{u_\tau}{\kappa} \times ln(\frac{z}{z_0}) \qquad (4)$$

A Logarithmic wind velocity profile is prescribed for the precursor simulations where the profile is generated using a wall-function based on the rough wall-law with surface roughness length $z_0 = 0.02$. In atmospheric boundary layer (ABL) flow scenarios, the velocity seen by a wind turbine is not known a priori and prescribing the velocity at a specific height becomes challenging due to the influence of roughness and geostrophic wind on velocity. This is addressed by implementing a PID-based velocity controller, as introduced by Stipa et al. [24]. This controller allows convenient prescription of the wind speed of $8m/s$ in the streamwise direction at hub-height position in the wind turbine simulations for our case. The boundary layer is considered to develop in the entire domain height, without any presence of a capping inversion. The surface roughness value pertains to an area near open and flat terrain, specifically in an onshore configuration [25]. The precursor simulation employs a domain size of $Lx = 12D$, $Ly = 10D$, and $Lz = 10D$, which has been determined to restrict domain blockage effectively. The domain is discretized using a uniform Cartesian grid with a grid spacing of $\Delta x = 8m$. Periodic boundary conditions are enforced in both the streamwise (x) and spanwise (y) directions, facilitating the advancement of time over ten hours. The modified precursor is subjected to the wind turbine case with inflow-outflow boundary conditions in the x-direction. The linear shear velocity profile is capped at a height of 640m from the ground.

Case 4

The same logarithmic wind profile precursor generated in Case 3 is subjected on the wind turbine with inflow-outflow boundary conditions in the x-direction, periodic in the y-direction and the rough-wall law at the lower z and a slip wall at top z boundary.

3. Results

The first section provides a concise overview of the key features of precursor simulation characteristics. Subsequently, the study investigates the impact of different inflow conditions (presented in section 2.2) on turbine performance and wake dynamics.

3.1. Precursor results

The precursor simulation was performed over 45,000 seconds (around 150 characteristic eddy turnover times) with a timestep of 0.5 seconds to disperse all the startup transients in the flow. Figure 2 shows the mean profiles for the velocities and turbulence intensity variation along the height. It can be observed that the controlling action of the velocity controller assures, as expected, a velocity of $8m/s$ at hub height (i.e. 150m). The mean flow velocities converge more
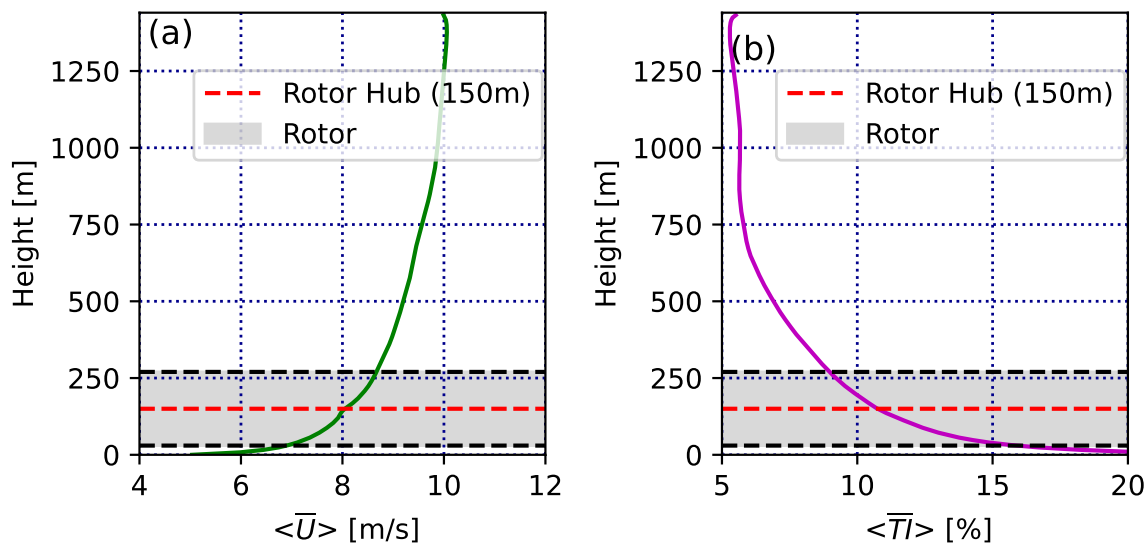
Figure 2: Variation of averaged velocity Fig(a) and averaged turbulence intensity Fig(b) along height (z).

Cases	Power			Thrust		
	Mean [MW]	Change in Power [%]	σ	Mean [MN]	Change in Thrust [%]	σ
1	5.78	-	0.1470	1.124	-	0.009732
2	5.75	- 0.49	0.1433	1.119	- 0.364	0.00968
3	6.3490	9.832	0.455	1.1609	3.28	0.031647
4	6.2475	8.075	0.520	1.1557	2.818	0.03656

Table 2: Mean values, percentage changes and standard deviations for power and thrust variations for different inflows from Case 1 to Case 4.

rapidly for the flow near the surface compared to the flow near the top of the boundary layer, where attaining a quasi-steady state solution requires a longer duration. The TI reaches its peak values near the wall, where turbulence is generated due to shear, and diminishes with height. The rotor experiences inflow TI levels ranging from 9% at the top to 15% at the bottom.

3.2. Turbine simulation results

3.2.1. Turbine performance Figure 3 presents the temporally averaged variation of the angle of attack, mean and r.m.s. values for both lift and drag along the blade rotation for the four inflow conditions. The polar axis represents the azimuthal angle where top of the rotor is at 0 deg and the bottom of the rotor is at 180 deg. The radial axis represents the radius of the rotor from $0m$ at center to $120m$ at the blade tip. It is clearly observed that the distribution of the angle of attack, mean and r.m.s. values for lift and drag are quite homogeneous for Case 1 in comparison to the sheared inflow cases. The angle of attack seems to have higher values at the top of the rotor for the case of linear shear and these values increase if turbulence is added. The

Test Case	Change in Power [%]	Change in Thrust [%]
WSC = 0	-	-
WSC = 0.05	-0.01	-0.02
WSC = 0.15	0.29	-0.05
WSC = 0.25	1.62	0.20

Table 3: Percentage change in power and thrust for WSC = 0 to WSC = 0.25 without inflow turbulence from Parinam et. al [8] presented for comparison.

higher angle of attack corresponds to higher velocities of the incoming flow, corresponding to higher mean lift and drag as well. Since rpm and pitch are constant, fluctuations in the lift force directly correspond to changes in torque. Consequently, this variability impacts the turbine's power output.

The higher angle of attack observed in sheared inflow cases could be linked to higher mean and percentage changes in power and thrust production, presented in Table 2. The power and thrust are increased by around 9 and 3 percent between Cases 2 and 3, respectively. This shows the impact of turbulence on power production and turbine loading for the selected wind speed. This can be compared with the findings of Parinam et. al [8] presented in Table 3. It can be seen that the power flips between linear shears of WSC = 0.15 and WSC = 0.25. This variation can be attributed to the transition between dominant impact of high shear versus the AoA variations. The latter leads to operation of the rotor blade away from the design point, where the airfoils are less performing. The variations in mean lift and drag are correlated to the AOA variations.

Figure 4 presents the radial profiles of mean and r.m.s for lift and drag. It can be observed that the mean and r.m.s of the lift variation are quite significant in comparison to the drag variations along the rotor blade. The mean drag along the blade is quite similar for all the 4 cases and the r.m.s. of the drag varies significantly until the $r/R = 0.3$ section of the blade which could be attributed to the actuator line modelling at the nacelle section. On the other hand, the r.m.s. of the lift profiles shows a significant variation along the whole blade for the four cases and may be attributed to the presence of turbulence. The presence of turbulence increases the mean angle of attack as can be seen for Cases 3 and 4 in comparison to Cases 1 and 2. This turbulence can be discerned in the r.m.s. values of lift and drag, where, for Case 3, the lift and drag variations are lower than for Case 4. Much of the rotor faces a turbulent inflow for Case 4 compared to Case 3. For the latter, the r.m.s. values are comparatively more uniform. This hints to a higher power output for Case 3 compared to Case 4.

3.2.2. Wake structure Figures 5 illustrate the vorticity magnitude, providing insights into the flow field under the inflow conditions outlined in Table 1 on the mid-span y-normal plane. The first difference that can be observed is the presence of turbulent structures in the inflow for Cases 3 and 4 in comparison to Cases 1 and 2. The turbulence in the inflow causes the vertical structures to breakdown leading to an early transition to a fully turbulent wake. It is clearly observed that, for Case 2, the presence of shear causes the tilting of the wake with the vertical structures at the top having higher velocities than those at the bottom. The vorticity level distribution also shows a dichotomy between low and high shears. With no shear, the vorticity levels are identical between the top and bottom streams. By contrast, the vorticity levels are higher in the top streams compared to bottom streams for sheared inflows. For Case 3, the presence of turbulence with linear shear causes earlier breakdown than for Case 2, at around
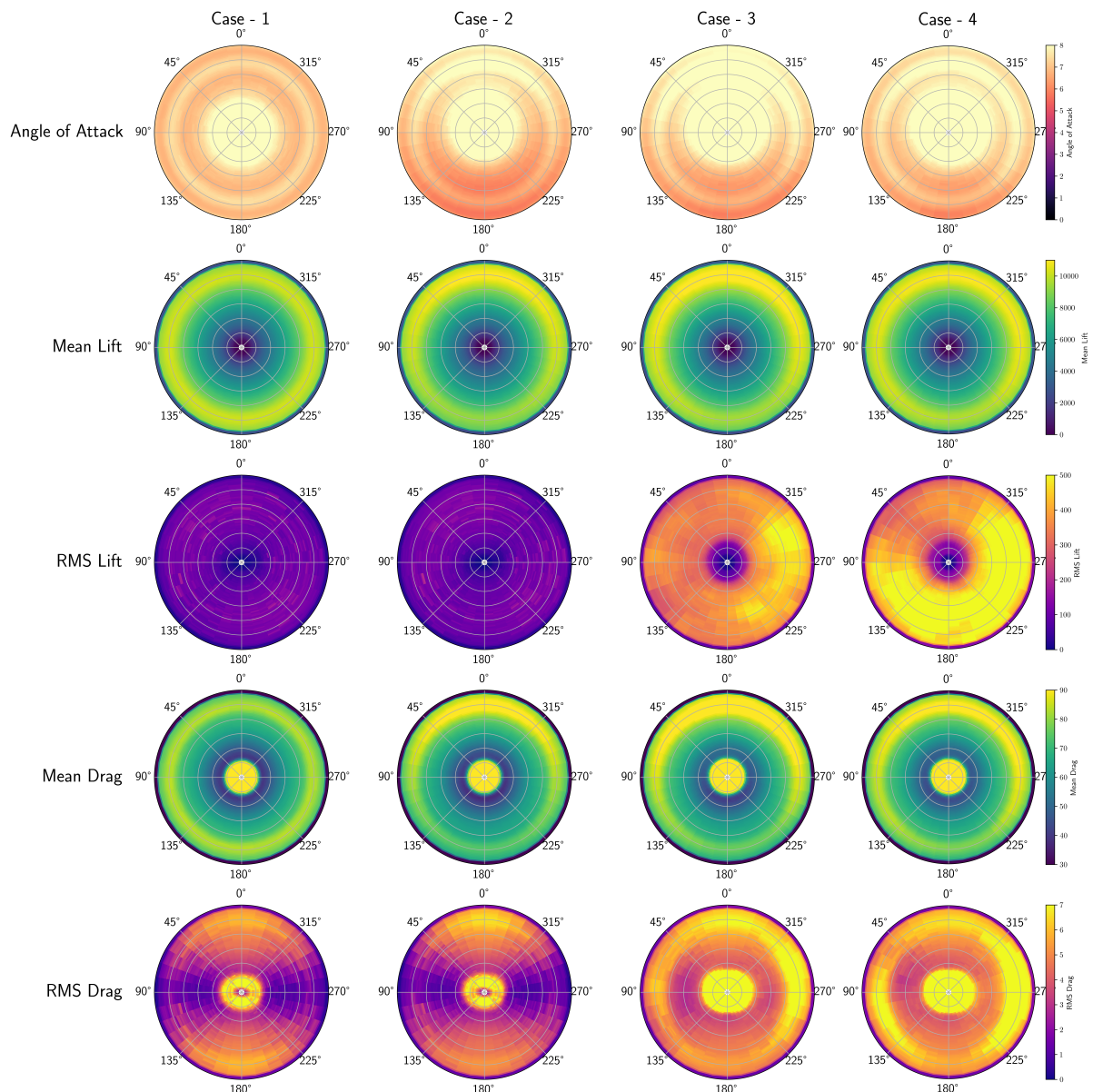
Figure 3: Temporal averaged azimuthal variation maps along the blade rotation for Angle of Attack, mean lift, r.m.s. lift, mean drag, r.m.s. drag for Cases 1–4.

0.5D behind the rotor and then the mixing of the flow starts. Similar behavior is observed for Case 4. For Case 4 , the influence of the wall law can be observed by having higher vorticity near the wall compared to Case 3. This seems to impact the rotor bottom stream, which breaks down even before 0.5 D and might be hinting to increased mixing in that region. Overall, qualitatively, the wake turbulence transition length, where there is lot of mixing and small-scale breakdown, is quickest for Case 4 around 0.4 D and highest for the no-shear case around 4 D.

3.2.3. Velocity distributions Figures 6 and 7 present the evolution of the flow over different upstream and downstream locations of the rotor plane in the streamwise directions using the profiles of time-averaged and r.m.s. velocities. The location -1D presents the initial undisturbed
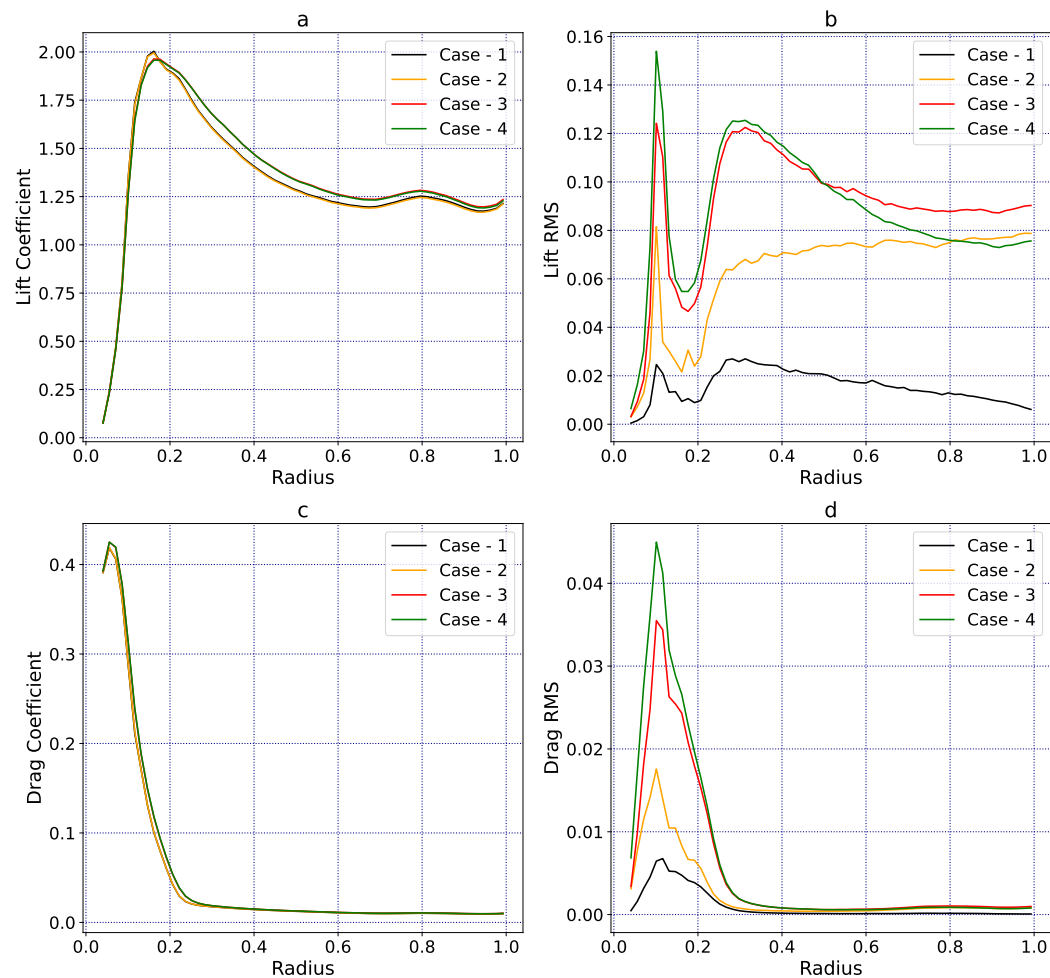
Figure 4: Radial profiles along the blade for mean lift, r.m.s. lift, mean drag, r.m.s. drag for Cases 1–4.

velocity profiles for different inflow conditions upstream of the rotor. It can be observed that the inflow conditions have the velocity profiles as intended, with Case 1 having a uniform inflow, Case 2 having linear shear, Case 3 is linear shear with turbulence and Case 4 uses the logarithmic law and turbulence. The rotor is located between -0.5 D and 0.5 D along the z/D direction and at 0D in the (x/D) streamwise direction. The effect of shear and logarithmic profile can be clearly seen from 0D to 1D, where the mean velocity profile starts to tilt according to the shear. At the 0D rotor location and 1D downstream of the rotor, the mean velocities for Case 2 and Case 3 are very similar showing that the effect of turbulence in the very near wake is not significant. Further downstream, between 3D and 5D, the effect of turbulence starts coming into play and increases the wake mixing. This may hint to a quicker wake recovery for the cases with turbulence which we would comment on in detail using the r.m.s. plots. Beyond $5D$, breaking down of large-scale structures into smaller structures following the turbulent kinetic energy cascade leads to the increase of turbulence in the flow for Cases 1 and 2, and consequently, of the velocity fluctuations. At -1 D location, the r.m.s. profiles show the presence of turbulence
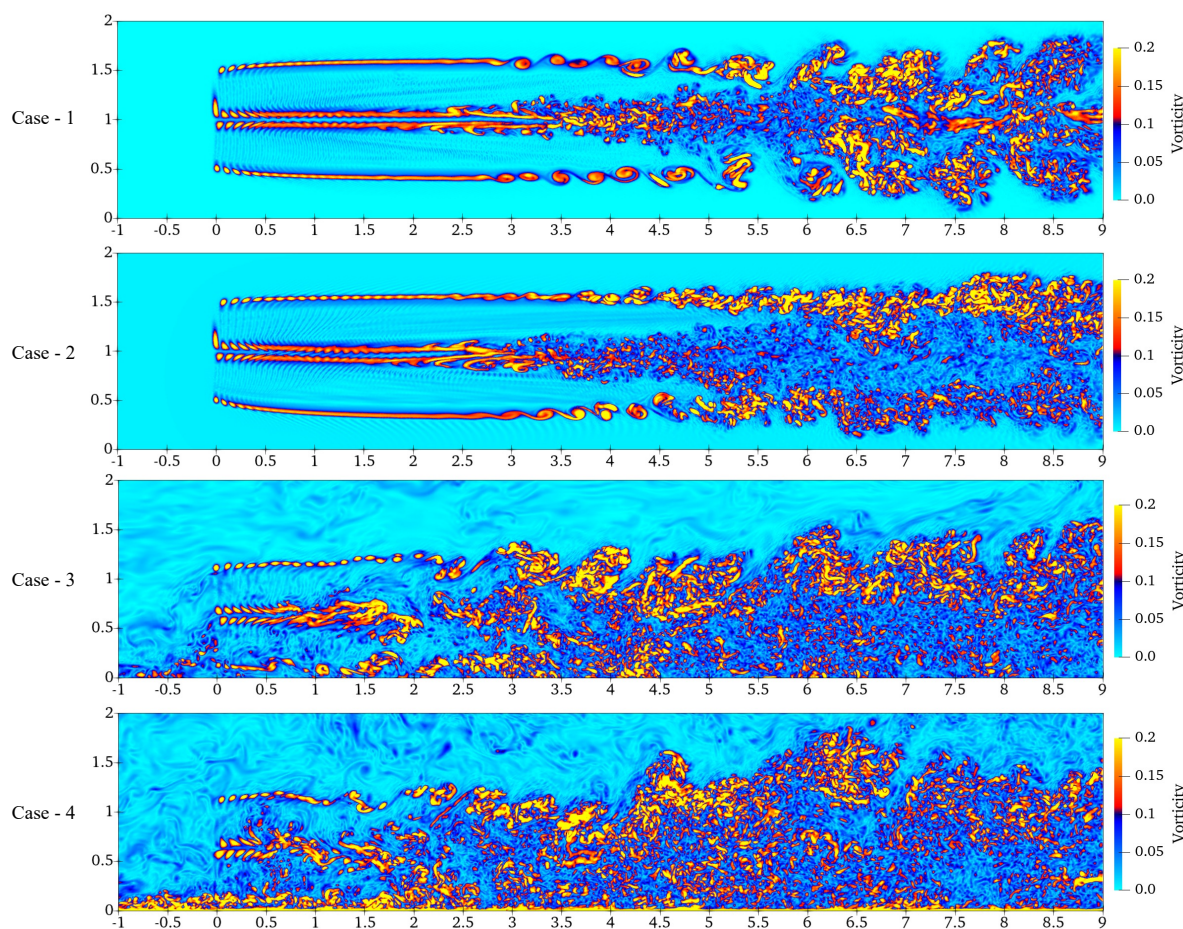
Figure 5: Streamwise vorticity contours in the Y-plane at mid-span for the inflow conditions from Table 1.

of similar order in the flow for both Cases 3 and 4. At the rotor location of 0D, all cases show the same level of turbulence. This shows that the influence of the rotor dominates that of the turbulence in the flow. From 0D to 3D the turbulence in the wake is much higher for Cases 3 and 4 than Cases 1 and 2. The r.m.s. plots show that the wake starts to recover by 4D for Cases 3 and 4. For Cases 1 and 2, the wake recovery is much slower and occurs around 6D which is supported by the findings of Parinam et al. [8].

The slight differences in the inflow turbulence levels for Cases 3 and 4 could be interpreted from the differences in variation of the normal components of the Reynolds stresses along the height z, as presented in Figure 8 for location -1D. The streamwise component uu/U_{hub} turbulence levels are quite similar for both cases. The higher values of the other two components vv/U_{hub} and ww/U_{hub} for Case 4 compared to Case 3 can be attributed to the boundary conditions. The presence of the wall generates turbulence in Case 4 whereas Case 3 has slip walls that do not add to turbulence production. This might cause some of the turbulent fluctuations to die out in Case 3 and, hence, the slight difference in inflow turbulence.

4. Conclusions
We performed high-resolution LES of the wake generated by the IEA 15MW reference wind turbine subjected to four different sheared inflow conditions. A precursor simulation was used to
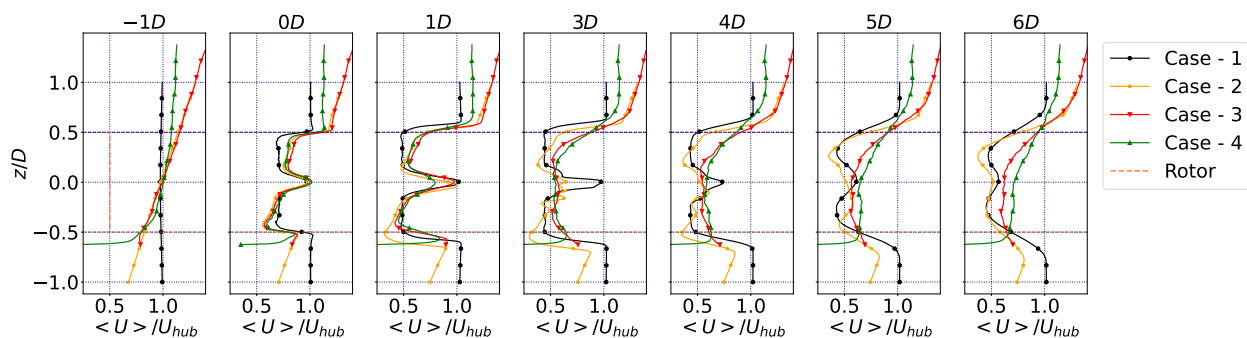
Figure 6: Mean streamwise normalised velocity profiles along the height z for different inflow cases presented in Table 1.
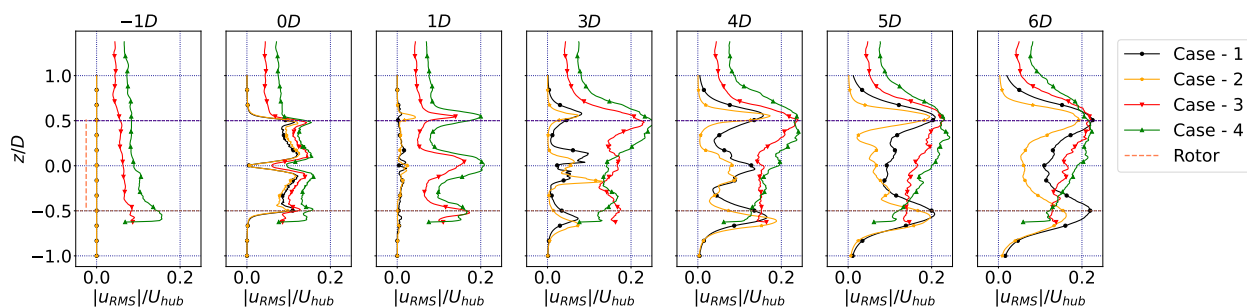

Figure 7: RMS of normalised velocity profiles along the height z for different inflow cases presented in Table 1.
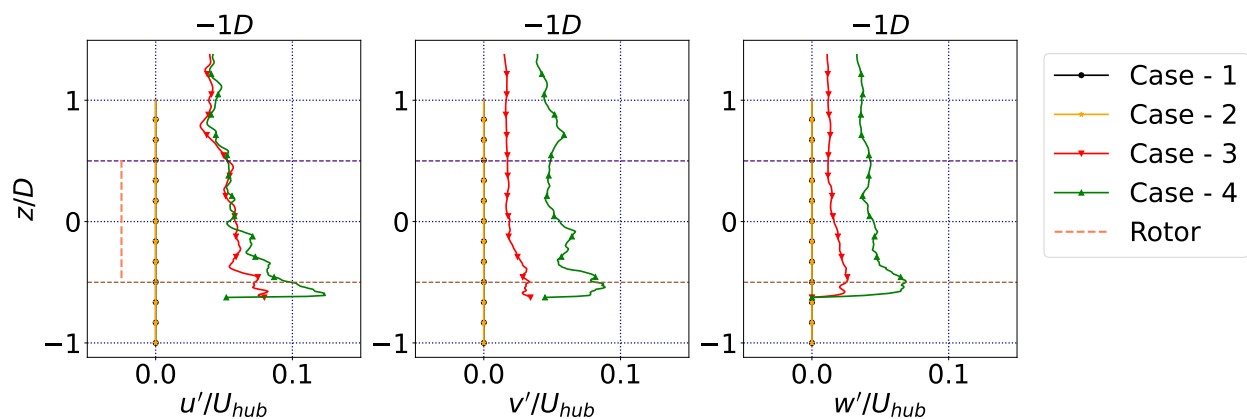

Figure 8: Diagonal components of Reynolds stresses along height z for different inflow cases presented in Table 1.

generate the turbulent inflow conditions and the turbine was modeled using the ALM approach. A constant hub-height wind speed was maintained through a velocity controller.

In the turbine simulations, for the wind speed selected, the presence of turbulence in the inflow was increasing the power output from the turbine, It was also found that the presence of turbulence expedited the wake recovery process to around 1-1.5 D, whereas for non-turbulent

cases it occurred around 4 D behind the rotor. The work is intended to be extended to further analysis into the wake recovery, evolution and structure by selectively adding effects of Coriolis forces and thermal stratification.

Acknowledgments

References

[1] Stevens R J and Meneveau C 2017 *Annual Review of Fluid Mechanics* **49** 311–339 ISSN 1545-4479
[2] Porté-Agel F, Bastankhah M and Shamsoddin S 2020 *Boundary-Layer Meteorology* **174** 1 –59
[3] Sanz Rodrigo J, Chávez Arroyo R A, Moriarty P, Churchfield M, Kosović B, Réthoré P E, Hansen K S, Hahmann A, Mirocha J D and Rife D 2017 *Wiley Interdisciplinary Reviews: Energy and Environment* **6**
[4] Veers P and et al 2019 *Science* **366**
[5] Uchida T 2020 *Energies* **13** 1–31
[6] Gaunaa M, Troldborg N and Branlard E 2023 *Wind Energy Science* **8** 503–513
[7] Abkar M, Sharifi A and Porté-Agel F 2016 *Journal of Turbulence* **17** 420–441
[8] Parinam A, Benard P, von Terzi D and Viré A 2023 *Journal of Physics: Conference Series* **2505** 012039
[9] Hodgkin A, Laizet S and Deskos G 2022 *Journal of Physics: Conference Series* **2265** 022061
[10] Sezer-Uzol N and Uzol O 2013 *Wind Energy* **16** 1–17
[11] Park J, Basu S and Manuel L 2014 *Wind Energy* **17** 359–384
[12] Gadde S N and Stevens R J A M 2021 *Phys. Rev. Fluids* **6**(1) 014603
[13] Strickland J M, Gadde S N and Stevens R J 2022 *Renewable Energy* **197** 50–58
[14] Wagner R, Courtney M, Gottschall J and Lindelöw-Marsden P 2011 *Wind Energy* **14** 993 – 1004
[15] Zhang J, Chowdhury S and Hodge B M 2014 *32nd ASME Wind Energy Symposium*
[16] Zhang W, Markfort C D and Porté-Agel F 2012 *Experiments in Fluids* **52** 1219–1235
[17] Hansen K S, Barthelmie R J, Jensen L E and Sommer A 2012 *Wind Energy* **15** 183–196
[18] Moureau V, Domingo P and Vervisch L 2011 *Comptes Rendus Mécanique* **339** 141–148 ISSN 1631-0721 high Performance Computing
[19] Houtin-Mongrolle F, Bénard P, Lartigue G and Moureau V 2021 *Journal of Physics: Conference Series* **1934** 012011
[20] Sørensen J N and Shen W Z 2002 *Journal of Fluids Engineering* **124** 393–399 ISSN 0098-2202
[21] Gaertner E, Rinker J, Sethuraman L, Zahle F and et al 2020 *NREL/TP-75698*
[22] Hsieh A S, Brown K A, deVelder N B, Herges T G, Knaus R C, Sakievich P J, Cheung L C, Houchens B C, Blaylock M L and Maniaci D C 2021 *Journal of Wind Engineering and Industrial Aerodynamics* **218**
[23] Emeis S and Turk M 2007 *Wind Energy* 61–64
[24] Stipa S, Ajay A, Allaerts D and Brinkerhoff J 2023 *Wind Energy Science Discussions* **2023** 1–41
[25] Burton T, Jenkins N, Sharpe D and Bossanyi E 2011 *Wind Energy Handbook* pp. 9–38
[26] Delft High Performance Computing Centre (DHPC) 2022 DelftBlue Supercomputer (Phase 1) `https://www.tudelft.nl/dhpc/ark:/44463/DelftBluePhase1`